Fuel 394 (2025) 135097

Contents lists available at ScienceDirect

Fuel

journal homepage: www.elsevier.com/locate/fuel

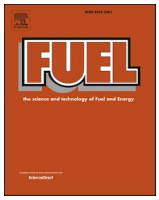

Full Length Article

Soot particles generated by *n*-heptane and *n*-heptane/OME_3 in an inverse diffusion flame: A comparative analysis of physical properties and oxidative reactivity

Ye Liu [a,b], Ran Zhang [c,1], Chenxi Wang [a,b,*], Haibo Chen [b], Gang Lyu [a,*], Jun Wang [c], Huayu Tian [c], He Yang [c], Yajun Wang [c], Chenyang Fan [d], Bin Xu [d], Xiaowei Wang [e], Hongyuan Wei [e], Dimitris Margaritis [f]

[a] State Key Laboratory of Engines, Tianjin University, Tianjin 300072, China
[b] Institute for Transport Studies, University of Leeds, Leeds LS2 9JT, UK
[c] SINOPEC Research Institute of Petroleum Processing Co., LTD., Beijing 100083, China
[d] Henan Provincial International Joint Laboratory of Energy Conservation and Pollutant Control of Energy Power Equipment, College of Vehicle and Traffic Engineering, Henan University of Science and Technology, Luoyang 471003, China
[e] CATARC Automotive Test Center (Tianjin) Co., Ltd., Tianjin 300300, China
[f] Centre for Research and Technology Hellas (CERTH), Hellenic Institute of Transport (HIT), 6th km Charilaou-Thermi, 57001 Thermi, Thessaloniki, Greece

ARTICLE INFO

Keywords:
E-fuel
Soot particles
Inverse diffusion flame
Physical properties
N-heptane

ABSTRACT

The widespread adoption of E-fuel, oxymethylene ether-3 (OME_3), is a promising solution to accelerate the decarbonisation of the transport sector. However, the application of OME_3 inevitably alters the combustion characteristics, affecting the soot generation process and consequently changing the physical properties of these soot particles. These alterations, in turn, influence not only associated health and climate concerns but also the control strategies of diesel particulate filter (DPF) regeneration. Here, high-resolution transmission electron microscopy (HRTEM) and thermogravimetric analysis (TGA) were employed to explore the effects of blending OME_3 on soot primary particle size, fractal dimension, nanostructure, and oxidative characteristics. The results show that the addition of OME_3 form smaller soot precursors and accelerates the oxidation of soot particles, which subsequently reduces the size of primary particles. The smaller size of soot particles favours oxidation, but they are likely to pose more severe health risks. The smaller primary particles exhibit more pronounced Brownian motion and weaker van der Waals forces, leading to the formation of a looser agglomerate structure and smaller fractal dimensions (D_f). Furthermore, the addition of OME_3 results in a reduction of long-range order in C atoms network and an increase of odd-number carbon rings during the generation of soot particles, which in turn leads to a reduction in fringe length (L_f) and an increase in fringe tortuosity (T_f) and separation distance (S_f) of soot particles. These nanostructural changes induced by OME_3 enhance the oxidative reactivity of soot particles, as evidenced by the lower oxidative characteristic temperatures and reduced activation energy.

1. Introduction

Traffic-related CO_2 emissions accounted for 24 % of the global total CO_2 emissions from fuel combustion in 2019, with road transport contributing approximately 74 % of this share [1]. Despite ongoing efforts to improve thermal efficiency and fuel economy, the increasing number of internal combustion engine vehicles (ICEVs) still leads to a continuously grow in CO_2 emissions each year. [2]. Given the carbon–neutral nature of E-fuels driven from CO_2-captured techniques, their application in ICEVs could significantly contribute to achieving carbon neutrality. Among the various E-fuels, oxymethylene ethers (OME_x) have demonstrated exceptional potential. First, OME_x can be synthesized by recycling CO_2 through electrochemical methods powered by clean energies, thus achieving a carbon balance [3]. Second, the OME_x blends easily with diesel without requiring modifications to the ICEVs [4]. Third, the high oxygen content and reduced C–C bonds in

* Corresponding authors.
E-mail addresses: c.wang2@leeds.ac.uk (C. Wang), lvg@tju.edu.cn (G. Lyu).
[1] Ran Zhang is also a co-first author due to his equal contribution to this work with Ye Liu.

https://doi.org/10.1016/j.fuel.2025.135097
Received 14 November 2024; Received in revised form 12 March 2025; Accepted 13 March 2025
Available online 20 March 2025

oxygenated OME_x fuels facilitate the suppression of soot precursor formation, thereby reducing soot particle emissions [5].

Among the OME_x (x = 1–5) fuels, OME_3 demonstrates superior potential in real-world application, with a suitable cetane number of 78, melting point of −41°C, and boiling point of 156°C [6]. The physical properties of OME_3 confer it with better storage capacity compared to OME_1, higher safety over OME_2, and superior low-temperature fluidity relative to OME_x (where x > 4) [7,8]. Therefore, the application of OME_3 in diesel additives has attracted significant attention [5,9,10]. However, it is important to note that OME_3 is not a carbon-free fuel; both pure OME_3 or diesel/OME_3 blend fuels inevitably generate particulate matter (PM). Previous research has demonstrated the advantages of OME_n fuels in reducing PM emissions. For instance, Arias et al. [11] investigated the impact of substituting diesel with OME_3 in an Euro 6 engine. They found that a 20 % OME_3 blend could reduce 61 % particle number emissions for the WLTC condition. Similarly, García-Oliver et al. [12] pointed out that adding over 30 % OME_3 to diesel changes combustion characteristics and significantly reduces soot particle emissions. Schmitz et al. [13] observed that the addition of OME_3 in premixed flames significantly reduces the emissions of larger soot particles. Existing studies mainly focus on the potential of OME_3 blends to reduce soot particle emissions. However, research on how OME_3 blends influence the soot physical properties remains limited.

The soot physical properties influence not only the environment and human health but also the efficiency of DPF regeneration. For instance, soot particle size and fractal dimension affect atmospheric residence time and transport, while soot nanostructure influences oxidative reactivity and the oxidative rate during DPF regeneration [14–16]. Soot particles with a more disordered nanostructure tend to oxidise more readily, enhancing DPF regeneration efficiency [17]. Conversely, highly ordered soot structures may resist oxidation, impeding regeneration processes [18]. Consequently, an in-depth understanding of the mechanisms by which OME_3 addition influences the physical properties of soot particles is crucial for mitigating adverse health effects and optimising control strategies of DPF regeneration.

Given these identified research gaps mentioned above, this research systematically examined the effects of OME_3 addition on the soot physical properties. In terms of ICEVs, isolating specific parameters is challenging because of the extremely complex thermal and dynamic processes involved. To achieve more controlled experimental conditions, an inverse diffusion flame was therefore employed in this research, as it enables more precise control over combustion parameters, allowing for a deeper understanding of the effects of OME_3 addition on the soot physical properties. In the tests, soot particles were collected at three varying heights above the burner (HAB), representing the phases of soot formation, growth, and oxidation. High-resolution transmission electron microscopy (HRTEM) and thermogravimetric analysis (TGA) were employed to characterise the physical properties and oxidative reactivity of soot particles, involving soot particle size, fractal dimension, fringe length, tortuosity, separation distance, oxidative characteristic temperatures and activation energy. The findings from this study are expected to provide a theoretical basis for the practical application of OME_3, contributing valuable insights into the broader adoption of e-fuels for sustainable transport solutions.

2. Experimental

2.1. Burner setup

To better understand soot properties in diesel engine combustion, the diffusion flame was used in this study as it exhibits similar characteristics to the primary combustion mode in diesel engines. Both involve a mixing-controlled combustion process, where fuel and air react at the flame front rather than being pre-mixed, making diffusion flames an effective platform for investigating soot formation, growth, and oxidation mechanisms under conditions relevant to diesel combustion. However, differences exist, such as pressure and turbulence levels, as diesel engines operate at high pressure with transient flow conditions, while the test burner operates at ambient pressure in a steady-state environment. Despite these differences, diffusion flames provide a controlled and reproducible setting, allowing for a detailed analysis of how fuel composition influences soot characteristics, which has been widely used in research [19,20]. As shown Fig. 1, the burner structure consists of three key components: 1) a 12.7 mm central tube designed for the oxygen and nitrogen gases, 2) a 30 mm intermediate annular porous plug for fuel delivery, and 3) a 75 mm outer porous plug used to serve as a shield to avoid secondary flames forming with ambient air. The burner was mounted on a vertical translation platform with a precision of ±0.005 mm, allowing for accurate control of the soot sampling position. The experiments were conducted at ambient pressure and a room temperature of 20 °C. The gas flow rates of O_2, N_2, and shielding N_2 were set to 0.52 L/min, 0.6 L/min, and 55 L/min, respectively. Additionally, a commercial fuel delivery system (Bronkhorst) was employed to continuously provide vaporised fuel with Ar (99.999 %) carrier to the burner through heated tubes maintained at 200 °C. The flow rates of both fuel and Ar were regulated using digital flow controllers (Bronkhorst), with precisions of 0.02 % and 0.2 %, respectively.

Considering OME_3's fast combustion speed, high cetane number, and tendency to increase NO_X emissions, its typical blending ratio in diesel engines without major modifications is usually kept below 30 % to maintain engine performance and emission compliance [21,22]. Given several studies investigated 10 % and 20 % OME_3 blending ratios [23,24]. Using the same blending ratios in this study contributes to a more comprehensive understanding of OME_3's impact by integrating findings from different perspectives, leading to a broader evaluation of its combustion and emission characteristics. Therefore, here, 10 % and 20 % OME_3 blending ratios (by substituting 10 % and 20 % of the total carbon content of *n*-heptane) were selected to explore the effects of OME_3 addition on soot particles, which designated as OME-10 and OME-20. After adding the OME_3, the overall vaporised fuel flow rate of carbon remains nearly constant. Table 1 provides the specific flow rates used in this study. The same approach was widely utilised for the analysis of other alternative fuels [25,26].

2.2. Soot sampling

As shown in Fig. 1, the stainless-steel probe sampler with a 0.15 mm sampling orifice downward to the flame was positioned horizontally directly above the flame. The sampling positions were the central axis of the flame with different HABs of 20, 40, and 60 mm, a Teflon filter was used to collected the samples used for TGA. To stopping subsequent chemical reactions during sampling, a cold nitrogen gas with 26.8 L/min flow rate was employed to cool and dilute the extracted gases. Further details on the probe sampling technique can be found in our previous studies [27–29]. After sampling sufficient soot particles, the samples were carefully gathered from the filter. Furthermore, the thermophoretic sampling method was employed to collect soot particles for the high-resolution transmission electron microscopy (HRTEM) analysis. This system was equipped with a linear electric cylinder (FESTO) with an acceleration above 100 m/s^2 and a top speed of 3 m/s, and the sampling time of soot particle was within 30 ms. The rapid sampling time can more accurately reflect the morphology of soot particles in the flame. In addition, the flame temperatures at different HABs were measured by an R-type thermocouple along the flame central axis. The recorded temperatures were corrected for radiative heat loss following the method outlined by Mcenally et al. [30]. Fig. 2 displays the measured temperatures at the three sampling locations. It can be seen that the difference in flame temperature was minimal after adding OME_3, indicating that the influence of OME_3 addition on combustion temperature is negligible.

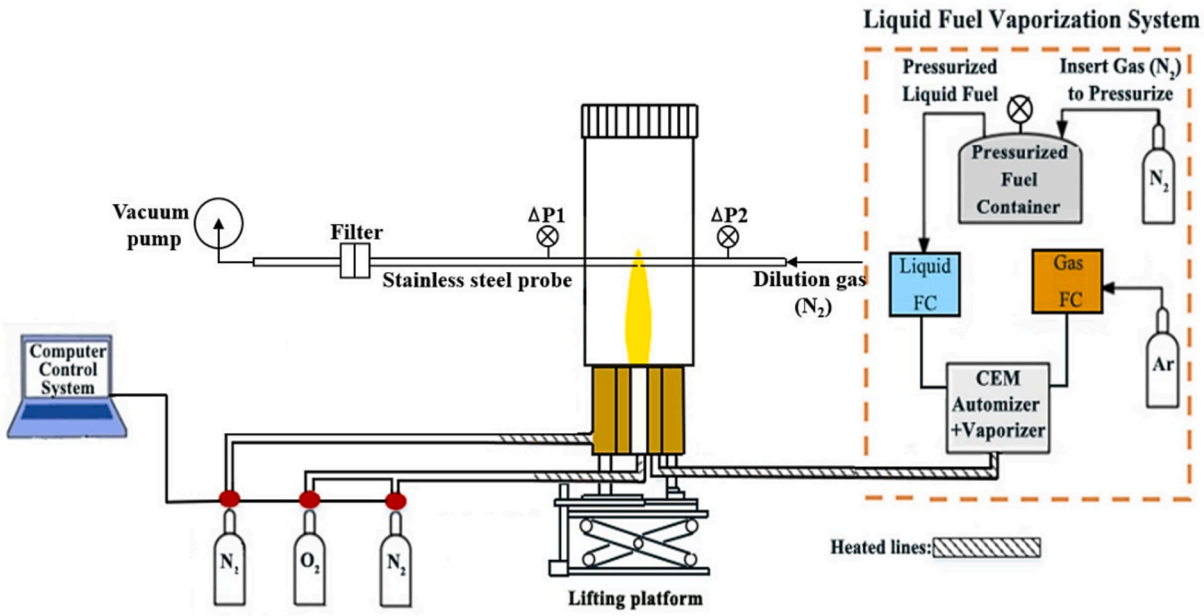

Fig. 1. Schematic diagram of experiment system.

Table 1
Parameters settings in the test.

Fuel	*n*-heptane	OME-10	OME-20
Flow rate of N_2 (L/min)	0.31	0.31	0.31
Mass flow rate of *n*-heptante (g/min)	1.17	1.05	0.93
Mass flow rate of OME_3 (g/min)	0	0.22	0.44
Carbon flow rate (g/min)	0.98	0.98	0.98
Flame height (mm)	70	68	65

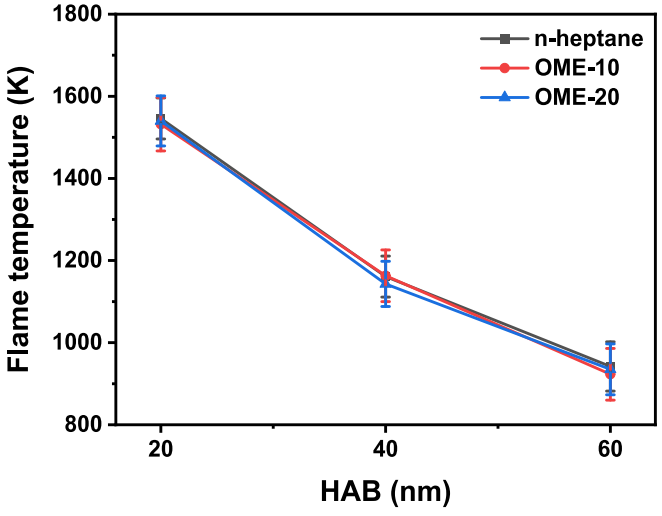

Fig. 2. Flame temperatures of different sampling positions.

2.3. Soot characterization

2.3.1. High-resolution transmission electron microscopy (HRTEM)

To explore soot morphology and nanostructure, HRTEM (EM-2010F) with magnification of 40,000× and 400,000× was employed. The TEM were used to determine the morphology parameters, including the number of primary particles (n_p), mean radius of gyration (R_g), and primary particle size (D_p), to calculate the fractal dimension (D_f). Taking the *n*-heptane soot at HAB = 20 mm as an example, the D_f was obtained from the slope of the scatter plot generated with log (R_g/D_p) on the x-axis and log (n_p) on the y-axis, as shown in Fig. 3. For each sampling HAB, more than 100 soot aggregates were selected to ensure statistical significance.

HRTEM images were employed to analyse nanostructure parameters, including fringe length (L_f), fringe tortuosity (T_f) and separation distance (S_f) using an automated fringe image processing system (FIPS). This FIPS involves image normalisation, selection of the region of interest, segmentation, enhancement, application of a Gaussian low-pass filter, binary conversion, skeletonisation, and calculation of the nanostructure parameters. Details of the image program are described in [31]. As shown in Fig. 4, the L_f was determined by converting the pixel count of each fringe to length based on a pixel size. The T_f was calculated as the ratio between the L_f and the distance connecting two endpoints. The S_f was determined by averaging the separation distances between the nearest points of each fringe pair.

2.3.2. Thermogravimetric analysis (TGA)

The oxidative reactivity of soot particles was evaluated using oxidative characteristic temperatures and activation energy (E_a)

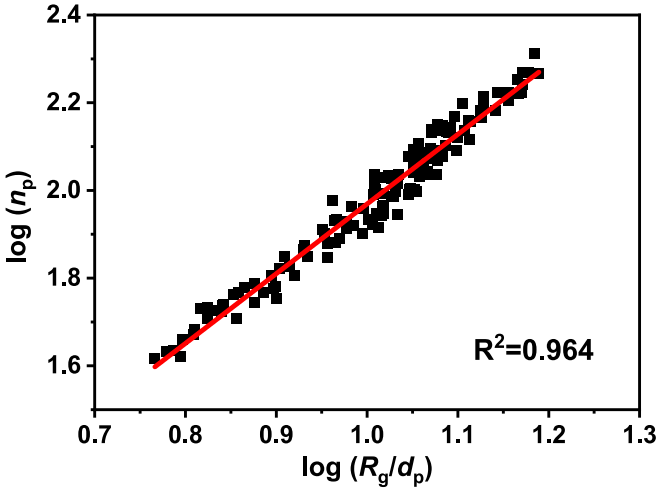

Fig. 3. Plot log (n_p) vs. log (r_g/d_p) of *n*-heptane soot sample.

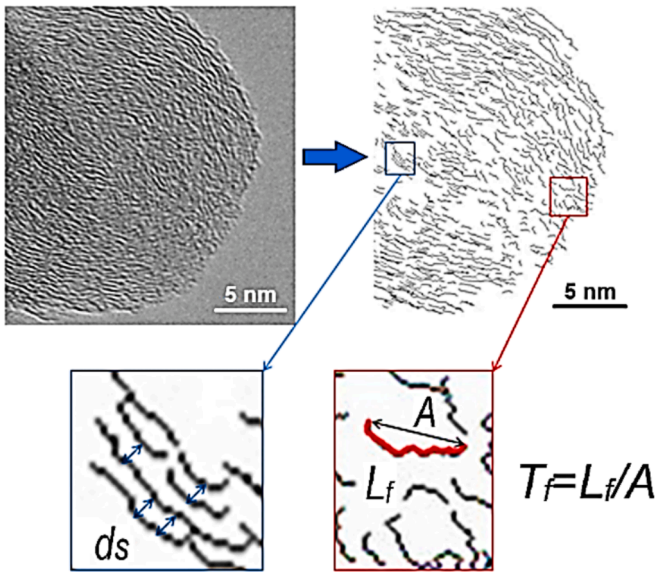

Fig. 4. Definition of soot nanostructure parameters.

through a thermogravimetric analyzer (TGA, Mettler-Toledo DSC1). The T_p is defined as the temperature when soot reaches its maximum oxidation rate during the temperature-programmed oxidation process at atmospheric pressure, and T_b is the temperature that 90 % soot mass is lost. The E_a reflects the minimum energy required for the reactants to transition from a stable state to an activated state, and the detailed process for calculating the E_a was reported in our previous work [32,33]. Before the experiment, the soot sample was heated to 773 K and maintained at this temperature for 60 min under a nitrogen atmosphere with a flow rate of 60 ml/min. After the temperature lowered to 473 K, soot sample was subjected to heating with a heating rate of 5 K/min to 1073 K in an air environment, maintained at a flow rate of 60 ml/min. In this study, the test of each sampling point was repeated three times to reduce experimental error.

3. Results and discussion

3.1. Size of primary particles

Fig. 5 shows the D_p under different HABs and OME_3 substituting proportions. It is evident that when HAB < 40 mm, the D_p for all soot samples exhibits an upward trend as the HAB increases. Conversely, when HAB > 40 mm, the D_p decreases with further increases in HAB.

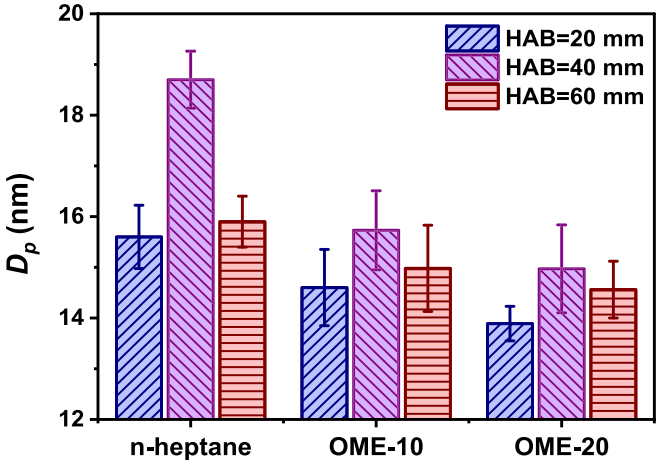

Fig. 5. Mean size of primary particles (D_p) from soot samples.

This phenomenon can be explained by the development stages of primary soot particles, which transition from a soot growth-dominant phase and an oxidation-dominant phase. The final diameter of the primary soot particles is the result of a competition between soot growth and oxidation [34]. During the soot growth-dominant phase, the growth rate of soot exceeds the oxidation rate, leading to an increase in the primary particle diameter. Conversely, during the oxidation-dominant phase, the oxidation rate surpasses the growth rate, causing a gradual reduction in the primary soot particle diameter. Therefore, based on the variation in particle size at different HABs, it can be inferred that soot growth is the dominant process when HAB increases from 20 mm to 40 mm. However, as the HAB further elevates from 40 mm to 60 mm, longer residence time of soot in flame makes oxidation becomes the prevailing process.

In addition, with the increase of OME_3 substituting proportion, the D_p of samples at the same HAB gradually decrease. The D_p range decreases from 15.6-18.7 nm to 13.9–15.0 nm when OME_3 substituting proportion increases from 0 to 20 %. This phenomenon indicates that the addition of OME_3 could distinctly reduce the size of primary soot particles. This variation may be mainly attributed to differences in soot formation and oxidation caused by the addition of OME_3. On the one hand, the higher oxygen content in OME_3 increases the air/fuel stoichiometric ratio for combustion, promoting more complete combustion and the formation of smaller soot precursors, such as acetylene or polycyclic aromatic hydrocarbons (PAHs), which subsequently inhibit the growth of soot particles [35]. On the other hand, the addition of OME_3 facilitates the formation of more oxygenated functional groups on soot surfaces, which accelerates the oxidation of soot particles and reduces the size of primary particles [36,37]. The primary soot particle with smaller D_p has a relatively large specific surface area which provides more active sites, thereby contributing to improving the oxidative reactivity [38]. Furthermore, the reduction in D_p increases the probability of the carbon layer collapsing into shorter fringes, which become intertwined with amorphous carbon, ultimately facilitating exfoliation, layer delamination, or internal combustion, contributing to the oxidation of soot particles [39]. Therefore, the small primary soot particles generated by OME_3-containing fuels would have higher oxidative reactivity.

Although the smaller size of soot particles is more susceptible to oxidation, it is worth noting that these smaller soot particles may also exhibit increased toxicity and pose serious harm to human health. This is primarily attributed to the enhanced capacity of smaller soot particles to promote the formation of reactive oxygen species (ROS) in both acellular and cellular environments, subsequently leading to oxidative stress [40]. Gren et al. [41] found that primary soot particles with a diameter less than 16 nm exhibit approximately 10 times the ROS formation potential compared to particles with a diameter above 20 nm. This significant difference is because smaller particles correspond to larger surface area, promoting the generation of free radicals, thus inducing oxidation stress, inflammation and enhancing genotoxicity [42,43]. Moreover, smaller soot particles can deposit more into the alveoli and further spread and penetrate distal organs through the bloodstream [44]. In addition, due to their reduced size, these particles are less likely to be effectively targeted and cleared by alveolar macrophages, leading to prolonged retention in the lungs and higher localised concentrations [45]. Consequently, the smaller soot particles caused by the addition of OME_3 may pose more significant risks compared to soot particles from pure petroleum fuels.

3.2. Fractal dimension

The D_f is typically used to quantify the compactness of soot aggregates. A higher D_f value indicates a more compact structure of soot aggregate, while a lower D_f value suggests a looser structure [32,40]. The D_f of soot samples with different HABs and OME_3 substituting proportions are displayed in Fig. 6. It can be seen that the D_f of soot

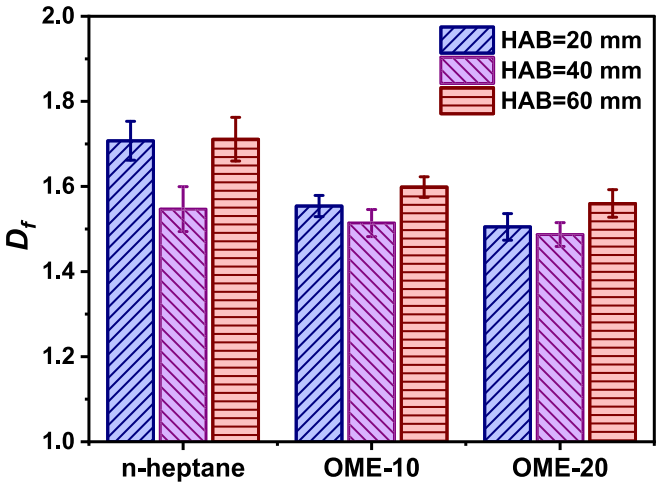

Fig. 6. Fractal dimension (D_f) of soot samples.

particles from all soot samples decreases initially and then increases with increasing HAB. This interesting phenomenon suggests that the degree of soot aggregation undergoes a decreasing and then increasing change as the HAB increases. This phenomenon can be attributable to the fact that, at lower HABs, the shorter residence time of soot within the flame is not conducive to the formation of chain-like structures [46]. As the HAB elevates to 40 mm, the continued coagulation of primary soot particles promotes the formation of more long-chain soot agglomerates. Furthermore, the decrease in flame temperature with increasing HAB further suppresses the agglomeration of soot particles, causing a decrease in D_f [47]. When the HAB is elevated to 60 mm, despite the further reduction in flame temperature, the soot aggregates undergo a longer residence time in the flame, allowing for a higher degree of agglomeration among the soot particles [48].

In addition, it can be seen from Fig. 6 that the D_f of soot aggregate from *n*-heptane varies within the range of 1.547 to 1.711 as the HAB changed, while the range of OME-20 only is 1.487 to 1.560. The gradual decrease in D_f with the addition of OME_3 indicates that the soot aggregates formed from OME_3-containing fuel have a looser structure. The reduction in D_f caused by the introduction of OME_3 can be explained by the following aspects. First, the soot particles generated from blending OME_3 have relatively smaller D_p. According to the diffusion-limited agglomeration mechanism, the soot particles with small sizes exhibit more pronounced Brownian motion. This increases the random motion of soot particles during the diffusion process prevents them from stacking in a tightly packed manner, leading to the formation of a looser agglomerate structure [49]. Moreover, smaller particles tend to be subjected to weaker van der Waals forces, making them more tend to form loose structures upon collision [50]. As looser aggregate structures typically exhibit larger specific surface area and more active sites, the soot aggregates generated by OME_3-containing fuel have higher oxidative reactivity [51,52].

It is worth noting that, soot also acts as an efficient absorbing medium, with its absorption–emission heat exchange capacity closely related to the D_f [53,54]. Liu et al. [55] found that as soot aggregates D_f decreases, their scattering cross-section significantly reduces. This reduction is caused by the looser chain-like structure of the aggregates, which weakens scattering interaction among soot particles. As a result, the smaller scattering cross section of soot implies a reduced capacity to reflect solar radiation, leading to more heat reach the earth's surface [56]. Thus, soot particles generated from OME_3-containing fuels, with the smaller D_f, may have weaker scattering capacity, potentially increasing solar radiation and contributing to climate warning.

3.3. Soot nanostructure

HRTEM analysis was conducted to illuminate the effects of OME_3 on soot nanostructure. Fig. 7 presents representative morphology images of *n*-heptane and *n*-heptane/OME_3 soot samples. As far as HRTEM images are concerned, the fringe are actually projections of graphene layers, and thus the fringe characteristics reflect the properties of graphene layers [57].

To quantify the changes of soot nanostructure following the addition of OME_3, the L_f, T_f, and S_f, were calculated through lattice fringe analysis [33]. Fig. 8 shows the mean values of L_f, T_f, and S_f for different soot samples. From Fig. 8a, the L_f of *n*-heptane soot increases from 0.711 nm to 1.131 nm with an increase in HAB from 20 mm to 60 mm. However, the range of L_f reduces to0.581–0.829 when the OME_3 substituting proportion achieved 20 %, indicating the blending of OME_3 would suppress the growth of the fringe length. This phenomenon is likely attributed to the changes in sp^3 and sp^2 orbital hybridisation development within the internal structure of soot particles. Ferraro et al. [58] and our previous research [59] found that the incorporation of OME_3 increases the proportion of sp^3 hybridisation within soot particles. The sp^3-hybridised C atoms represent defect sites that can disrupt the sp^2-hybridised network, leading to a reduction in long-range order, which in turn results in a decrease in fringe length [37,60]. The graphene layers are composed of carbon atoms situated at basal plane and edge positions. The edge carbon atoms exhibit significantly higher reactivity than those in basal plane [61]. Generally, shorter fringes which means smaller graphene layers have a higher proportion of edge-positioned carbon atoms, resulting in the high oxidative reactivity. Furthermore, it was found that the L_f of all soot samples increased as the HAB elevated from 20 mm to 60 mm. The gradually growth of fringe length with elevating HAB are likely due to the longer residence time in flame and relatively lower flame temperatures at higher HAB [62]. A longer residence time promotes the hydrogen abstraction carbon addition reaction on soot surface, resulting in the growth of fringe length [63]. At the same time, a lower flame temperature slows down soot oxidation, leading to an increase in the L_f of all soot samples [62].

Fig. 8b depicts the T_f of soot samples. It can be seen that the T_f of *n*-heptane soot samples at different HABs is in the range of 1.366–1.291. As the OME_3 content increases to 20 %, the T_f range of soot particlesincreases to 1.445–1.345. This phenomenon may be attributed to the effects of OME_3 on forms of carbon atom in soot particles. In ideal graphite microcrystalline layers, the carbon atoms are in the form of a six-membered ring lamellar structure [64]. However, in practice, due to differences in the generation environments, gas phase components, and reaction pathways, a certain amount of odd-number carbon rings would form during the generation of soot particles, which lead to a certain curving of the microcrystalline layer [65,66]. The curved fringes facilitate the overlapping of electronic orbitals, increasing the C–C bond strain and weakening electronic resonance stabilisation, thereby making the C atoms more vulnerable to oxygen [67]. That is, the increase in fringe tortuosity of soot particles generally leads to higher oxidative reactivity. Furthermore, as illustrated in Fig. 8b, with the increase in HAB, the T_f of all soot samples shows a decreasing trend. According to the analysis presented in Section 3.1, this trend can be attributed to the progressive dominance of oxidation at higher HABs. Fringes with higher tortuosity exhibit reduced electronic resonance stabilisation, which renders them more susceptible to consumption during the oxidation phase [31,68]. Consequently, as the oxidation process dominates, the overall fringes gradually become a flatter with increasing HAB, thereby contributing to a reduction in T_f.

Fig. 8c displays the S_f variations of different soot samples with various OME_3 substituting proportions and HABs. The S_f range increases from 0.423-0.373 nm for *n*-heptane to 0.531–0.472 nm for OME-20 soot, suggesting that the soot transforms toward a more disordered structure after adding OME_3. This phenomenon is likely related to the reduction in L_f following the addition of OME_3. The L_f in HRTEM images reflects the

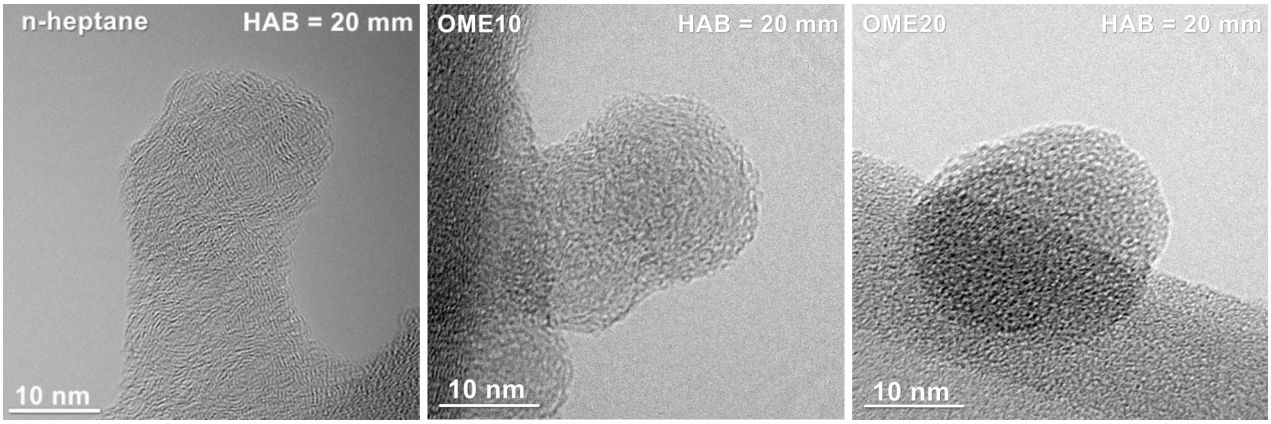

Fig. 7. Representive HRTEM images of *n*-heptane and *n*-heptane/OME_3 soot samples.

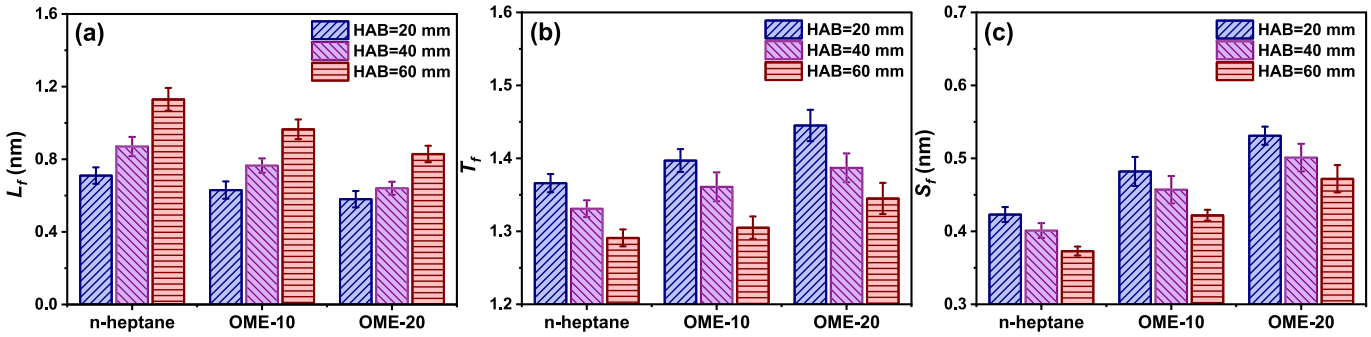

Fig. 8. Mean fringe length (L_f), fringe tortuosity (T_f) and separation distance (S_f) of soot samples.

size of the microcrystalline layer, with shorter L_f indicating smaller microcrystalline layer size in soot samples. The addition of OME_3 decreases the L_f, and the resulting smaller size of microcrystalline layers weakens the Van der Waals forces between layer planes, resulting in the increase of separation distance [69]. During the oxidation process of soot particles, gases diffuse through the continuous domains between microcrystalline layers. The larger interlayer spacing between these microcrystalline layers would reduce the resistance to gas diffusion and facilitate the diffusion of O_2 to the active sites, thereby the increased S_f caused by adding OME_3 favors the oxidation of soot particles [61,70]. In addition, when the HAB increased from 20 to 60 mm, the S_f of all soot samples presents a similar decreasing trend. This phenomenon suggests that the soot samples transform towards a more ordered structure with increasing residence time of soot in flame. This is likey because, with prolonged residence time, the L_f continues to increase, enhancing the interlayer forces between layars and bringing them closer together.

To comprehensively compare the nanostructural characteristics, the histograms and Gaussian fitting curves of the distributions of L_f, T_f and S_f were also analysed for soot samples at HAB = 20 mm. Fig. 9 shows the distribution characteristics of nanostructural parameters for n-heptane and n-heptane/OME_3 soot samples, where the bin widths are 0.1 nm for the L_f distribution, 0.05 for the T_f distribution and 0.0125 nm for the Sf distribution. Overall, the trend of peak variations for L_f, T_f and S_f distribution are similar to that of their mean values. Specifically, the L_f distribution of all soot particles is in the range of 0–2 nm, with approximately 75 % of the L_f in *n*-heptane soot particles being less than 0.8 nm. As the OME_3 blending ratio increases, the L_f distribution shifts toward shorter sizes, and about 75 % of the crystalline lengths are smaller than 0.7 nm for OME-20 soot particles. The T_f distribution is in the range of 0.8–2 for all soot particles. As the OME_3 blending ratio increases, the peak of the T_f distribution shows an increasing trend. The S_f distribution of soot particles shows significantly change with adding OME_3. The S_f distribution of *n*-heptane soot particles concentrated in the range of 0.35–0.55 nm, while that of OME-20 soot particles is concentrated in the range of 0.45–0.6 nm.

3.4. Oxidative reactivity

The results obtained from HRTEM analysis demonstrated that the blending of OME_3 resulted in a reduction in D_p, D_f, and L_f and an increase in T_f and S_f. These changes in physical properties are likely to enhance the oxidative reactivity of soot particles [63,65,66]. To further validate the influence of changes in soot physical properties on oxidative reactivity, the T_p, T_b, and E_a obtained from TGA analysis were employed to evaluate the oxidative characteristics of soot samples.

Fig. 10 illustrates the T_p and T_b values for soot samples. Both T_p and T_b decrease with increasing OME_3 substituting proportion. The maximum reductions of the T_p and T_b reach 28.6 °C and 36.4 °C, respectively, at HAB = 60 nm following the addition of OME_3. The lower T_p and T_b values suggest that the blending of OME_3 increases the soot oxidative reactivity, and lowers the difficulty of achieving soot oxidative removal, both of which are beneficial to the regeneration of deposited soot in DPF. Consequently, the addition of OME_3 can reduce the fuel required for active DPF regeneration and improve fuel economy.

In parallel, a decrease in the E_a, as depicted in Fig. 11, clearly demonstrates the effect of OME_3 on enhancing oxidative reactivity of soot particles. Specifically, at HAB = 20 nm, the E_a reduction after 20 % addition of OME_3 reaches 7.7 %. The maximum reduction is observed at HAB = 60 nm, with E_a decreasing by 14.6 %. These results further confirm that the physical properties variations of soot particles, such as D_p, D_f, L_f, T_f and S_f, induced by the introduction of OME_3, contribute to the enhancement in oxidative reactivity. In addition, the enhanced soot reactivity and oxidation behaviour difference have direct implications for diesel particulate filter (DPF) performance. The increased reactivity

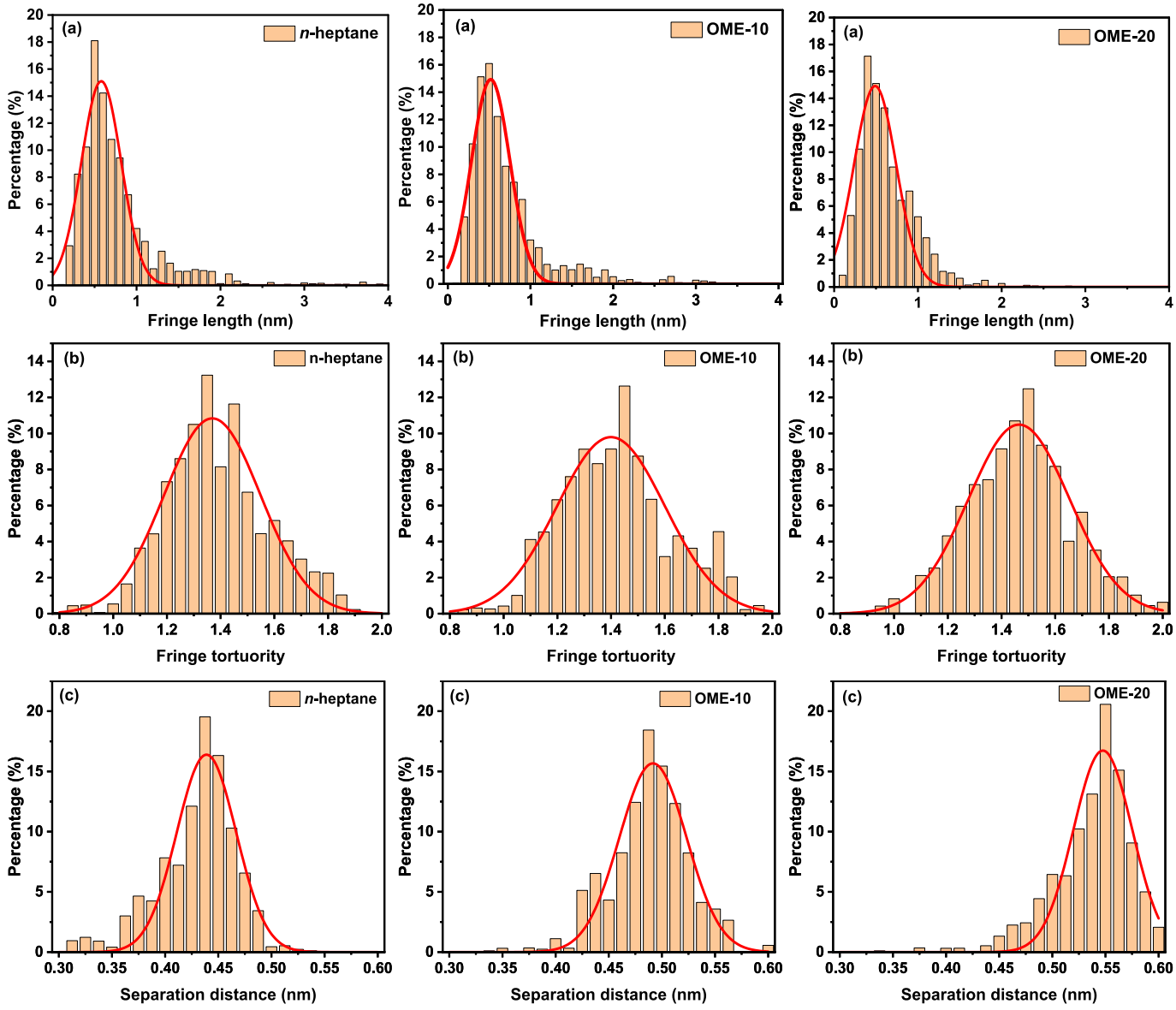

Fig. 9. Histograms of fringe length (L_f), fringe tortuosity (T_f) and separation distance (S_f) of soot samples at HAB = 20 mm.

suggests that soot from OME_3-containing fuels may oxidise more readily, potentially improving DPF regeneration efficiency. This could enable lower regeneration temperatures or shorter regeneration cycles, leading to reduced fuel consumption and extended DPF lifespan.

4. Conclusions

To clarify the effects of OME_3 addition on the physical properties and oxidative reactivity of soot particles, high-resolution transmission electron microscopy (HRTEM) and thermogravimetric analysis were used to explore the primary particle size, fractal dimension (D_f), fringe length (L_f), tortuosity (T_f), separation distance (S_f), and oxidative characterisitcs of *n*-heptane and *n*-heptane/OME_3 soot particles. The main conclusions of this study can be summarised as follows:

- The addition of OME_3 distinctly reduces the size of primary soot particles. Although the smaller size of soot particles promotes oxidation, they increase the likelihood of prolonged retention in the lungs, promoting oxidative stress, and thereby posing greater health risks.
- Soot aggregates from OME_3-containing fuels exhibit a smaller D_f than compared to those from *n*-heptane, which reduces the scattering capacity of soot particles, allowing more solar radiation to penetrate and potentially contributing to climate warming.
- The addition of OME_3 results in a reduction in L_f and an increase in T_f and S_f. These variations in soot nanostructure enhance oxidative reactivity, as indicated by lower oxidative characteristic temperatures and reduced activation energy. This indicates that adding OME_3 can facilitate more efficient regeneration of diesel particulate filters (DPF).

CRediT authorship contribution statement

Ye Liu: Writing – original draft, Visualization, Project administration, Methodology, Investigation, Formal analysis, Data curation, Conceptualization. **Ran Zhang:** Writing – review & editing, Resources. **Chenxi Wang:** Writing – review & editing, Visualization, Methodology, Investigation, Data curation, Conceptualization. **Haibo Chen:** Project administration, Funding acquisition. **Gang Lyu:** Writing – review & editing, Project administration. **Jun Wang:** Writing – review & editing. **Huayu Tian:** Data curation. **He Yang:** Data curation. **Yajun Wang:**

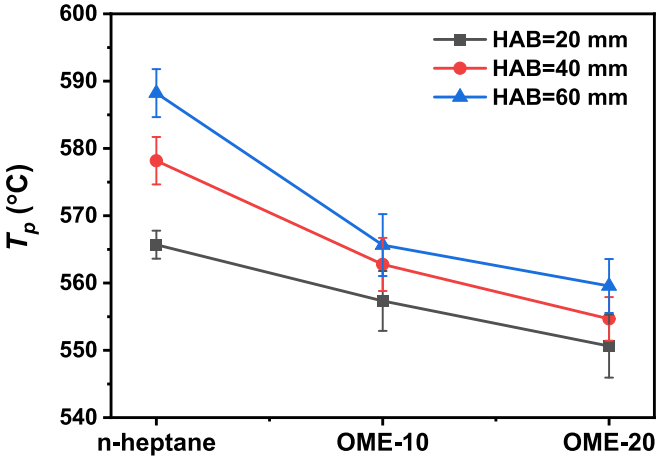

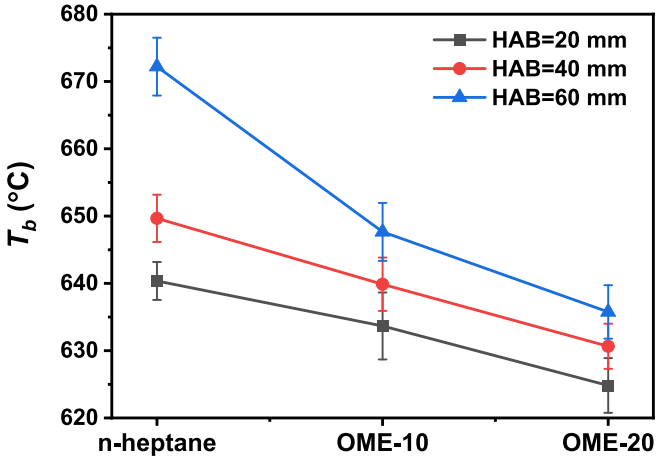

Fig. 10. Peak and burnout temperatures of soot samples.

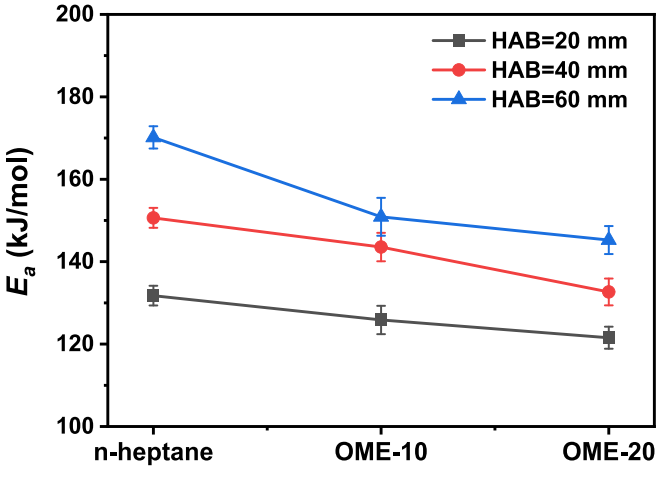

Fig. 11. Activation energy (E_a) of soot samples.

Writing – review & editing. **Chenyang Fan:** Writing – review & editing. **Bin Xu:** Writing – review & editing. **Xiaowei Wang:** Visualization, Investigation. **Hongyuan Wei:** Visualization, Investigation. **Dimitris Margaritis:** Writing – review & editing.

Declaration of competing interest

The authors declare that they have no known competing financial interests or personal relationships that could have appeared to influence the work reported in this paper.

Acknowledgments

This research is supported by the National Energy R&D Center of Petroleum Refining Technology (RIPP, SINOPEC, China), the EPSRC_IAA (No. 127410.050), and EU-funded projects nPETS (No. 954377).

Data availability

The authors do not have permission to share data.

References

[1] International Energy Agency. Tracking transport 2020. 2020, URL https://www.iea.org/reports/tracking-transport-2020.
[2] Pitsh H, Goeb D, Cai L, et al. Potential of oxymethylene ethers as renewable diesel substitute. Prog Energy Combust Sci 2024;104:101173.
[3] Cai L, Jacobs S, Langer R, et al. Auto-ignition of oxymethylene ethers (OMEn, n=2-4) as promising synthetic e-fuels from renewable electricity: shock tube experiments and automatic mechanism generation. Fuel 2020;264:116711.
[4] Tan YR, Salamanca M, Pascazio L, et al. The effect of poly (oxymethylene) dimethyl ethers (PODE3) on soot formation in ethylene/$PODE_3$ laminar coflow diffusion flames. Fuel 2021;283:118769.
[5] Pelerin D, Gaukel K, Hartl M, et al. Potentials to simplify the engine system using the alternative diesel fuels oxymethylene ether OME1 and OME3-6 on a heavy-duty engine. Fuel 2020;259:116231.
[6] He T, Wang Z, You X, et al. A chemical kinetic mechanism for the low- and intermediate-temperature combustion of Polyoxymethylene Dimethyl Ether 3 (PODE3). Fuel 2018;212:223–35.
[7] Zheng Y, Tang Q, Wang T, et al. Synthesis of a green fuel additive over cation resins. Chem Eng Technol 2013;36:1951–6.
[8] Rodríguez-Vallejo DF, Valente A, Guillen-Gosalbez G, et al. Economic and life-cycle assessment of OME_{3-5} as transport fuel: a comparison of production pathways. Sustainable Energy Fuels 2021;5:2504–16.
[9] Saupe C, Atzler F. Potentials of oxymethylene-dimethyl-ether in diesel engine combustion. Automot Engine Technol 2022;7:331–42.
[10] Omari A, Heuser B, Pischinger S, et al. Potential of long-chain oxymethylene ether and oxymethylene ether-diesel blends for ultra-low emission engines. Appl Energy 2019;239:1242–9.
[11] Arias S, Agudelo JR, Ramos A, et al. Emissions from a Euro 6 engine using polyoxymethylene dimethyl ethers: chemical effects vs mapping strategy. Fuel 2023;335:127017.
[12] García-Oliver JM, Novella R, Mico C, et al. A numerical investigation of the performance of oxymethylene ethers blended with fossil diesel to reduce soot emissions in compression ignition engines. Fuel 2022;324:124768.
[13] Schmitz R, Russo C, Ferraro F, et al. Effect of oxymethylene ether-2-3-4 (OME2-4) on soot particle formation and chemical features. Fuel 2022;324:124617.
[14] Song J, Alam M, Boehman AL, et al. Examination of the oxidation behavior of biodiesel soot. Combust Flame 2006;146:589–604.
[15] Li Z, Song C, Song J, et al. Evolution of the nanostructure, fractal dimension and size of in-cylinder soot during diesel combustion process. Combust Flame 2011;158(8):1624–30.
[16] Lee KO, Megaridis CM, Zelepouga S, et al. Soot formation effects of oxygen concentration in the oxidizer stream of laminar coannular nonpremixed methane/air flames. Combust Flame 2000;121(1–2):323–33.
[17] Khalid AQ, Boehman AL. Impact of exhaust gas recirculation (EGR) on the oxidative reactivity of diesel engine soot. Combust Flame 2008;155(4):675–95.
[18] Fang HL, Lance MJ. Influence of soot surface changes on DPF regeneration. SAE Technical Paper, 2004, 2004-01-3043.
[19] Bockhorn H. Soot formation in combustion: mechanisms and models. Berlin, Germany: Springer-Verlag; 1994.
[20] Pena JP, Raj A, Stephen S, et al. Physicochemical properties of soot generated from toluene diffusion flames: effects of fuel flow rate. Combust Flame 2017;178:286–96.
[21] Liu H, Wang Z, Wang J, et al. Performance, combustion and emission characteristics of a diesel engine fueled with polyoxymethylene dimethyl ethers (PODE3-4)/diesel blends. Energy 2015;88:793–800.
[22] Asad U, Ramos M, Tjong J. An investigation of OME_3-Diesel fuel blend on a multi-cylinder compression ignition engine. SAE technical paper, 2022, 2022-01-0439.
[23] Wang T, Liu J, Sun P, et al. Influence of injection parameters on combustion, gaseous emissions and particle size distribution of a CRDI diesel engine operating with PODE/diesel blends. Fuel 2020;281:118733.

[24] Iannuzzi SE, Barro C, Boulouchos K, et al. POMDME-diesel blends: Evaluation of performance and exhaust emissions in a single cylinder heavy-duty diesel engine. Fuel 2017;203(1):57–67.
[25] Tan YR, Botero ML, Sheng Y, et al. Sooting characteristics of polyoxymethylene dimethyl ether blends with diesel in a diffusion flame. Fuel 2018;224:499–506.
[26] Liu Y, Cheng X, Li Y, et al. Effects of ammonia addition on soot formation in ethylene laminar diffusion flames. Fuel 2021;292:120416.
[27] Liu Y, Song C, Lv G, et al. Virgin and extracted soots in premixed methane flames: a comparison of surface functional groups, graphitization degree, and oxidation reactivity. Energy Fuel 2017;31:6413–21.
[28] Wang HW, Huang ZH, Zhou LB, et al. Technical Note: investigation on emission characteristics of a compression ignition engine with oxygenated fuels and exhaust gas recirculation. Proc Inst Mech Eng D: J Automobile Eng 2000;214:503–8.
[29] Liu Y, Song C, Lv G, et al. Relationships between the electrical properties and nanostructure of soot particles in a laminar inverse diffusion flame. Proc Combust Inst 2019;37:1185–92.
[30] Mcenally CS, Koylu MO, Pfefferle LD. Soot volume fraction and temperature measurements in laminar nonpremixed flames using thermocouples. Combust Flame 1997;109(4):701–20.
[31] Yehliu K, Vander Wal RL, Boehman AL. Development of an HRTEM image analysis method to quantify carbon nanostructure. Combust Flame 2011;158:1837–51.
[32] Liu Y, Zhang X, Lyu G, et al. Effect of the oxidation-induced fragmentation of primary particles on soot oxidation reactivity. Combust Flame 2022;240:112026.
[33] Liu Y, Fan C, Wang X, et al. Thermally induced variations in the nanostructure and reactivity of soot particles emitted from a diesel engine. Chemosphere 2022;286:131712.
[34] Fan C, Song C, Lv G, et al. Impact of post-injection strategy on the physicochemical properties and reactivity of diesel in-cylinder soot. Proc Combust Inst 2019;37:4821–9.
[35] Pitsch H, Goeb D, Cai L, et al. Potential of oxymethylene ethers as renewable diesel substitute. Prog Energy Combust Sci 2024;104:101173.
[36] Soriano JA, Agudelo JR, Lopez AF, et al. Oxidation reactivity and nanostructural characterization of the soot coming from farnesane - A novel diesel fuel derived from sugar cane. Carbon 2017;125:516–29.
[37] Vander Wal RL, Bryg VM, Hays MDXPS. Analysis of combustion aerosols for chemical composition, surface chemistry, and carbon chemical state. Anal Chem 2011;83:1924–30.
[38] Lapuerta M, Oliva F, Agudelo J, et al. Effect of fuel on the soot nanostructure and consequences on loading and regeneration of diesel particulate filters. Combust Flame 2012;159(2):844–53.
[39] Vander Wal RL, Tomasek AJ. Soot oxidation: dependence upon initial nanostructure. Combust Flame 2003;134:1–9.
[40] Verma N, Pink M, Schmitz-Spanke S. A new perspective on calmodulin-regulated calcium and ROS homeostasis upon carbon black nanoparticle exposure. Arch Toxicol 2021;95:2007–18.
[41] Gren L, Malmborg VB, Jacobsen NR, et al. Effect of renewable fuels and intake O_2 concentration on diesel engine emission characteristics and reactive oxygen species (ROS) formation. Atmos 2020;11(6):641.
[42] Jiang N, Wen H, Zhou M, et al. Lowdose combined exposure of carboxylated black carbon and heavy metal lead induced potentiation of oxidative stress, DNA damage, inflammation, and apoptosis in BEAS-2B cells. Ecotoxicol Environ Saf 2020;206:111388.
[43] Ihantola T, Hirvonen MR, Ihalainen M, et al. Genotoxic and inflammatory effects of spruce and brown coal briquettes combustion aerosols on lung cells at the air-liquid interface. Sci Total Environ 2022;806:150489.
[44] Borm PJA, Schins RPF, Albrecht C. Inhaled particles and lung cancer, part B: paradigms and risk assessment. Int J Cancer 2004;110:3–14.
[45] Oberdörster G. Pulmonary effects of inhaled ultrafine particles. Int Arch Occup Environ Health 2000;74:1–8.
[46] Kellerer H, Koch R, Wittig S. Measurements of the growth and coagulation of soot particles in a high-pressure shock tube. Combust Flame 2000;120(1):188–99.
[47] Wei J, Song C, Lv G, et al. A comparative study of the physical properties of in-cylinder soot generated from the combustion of n-heptane and toluene/n-heptane in a diesel engine. Proc Combust Inst 2015;35(2):1939–46.
[48] Zhu J, Lee KO, Ahmet Y, et al. Effects of engine operating conditions on morphology, microstructure, and fractal geometry of light-duty diesel engine particulates. Proc Combust Inst 2005;30(2):2781–9.
[49] Friedlander SK. Smoke, dust, and haze: fundamentals of aerosol dynamics. Phys Today 1977;30(9):58–9.
[50] Koch W, Friedlander SK. The effect of particle coalescence on the surface area of a coagulating aerosol. J Colloid Interface Sci 1990;140(2):419–27.
[51] Zhang R, Zhang Y, Kook S. Morphological variations of in-flame and exhaust soot particles associated with jet-to-jet variations and jet-jet interactions in a light-duty diesel engine. Combust Flame 2017;176:377–90.
[52] Zhang Y, Kim D, Rao L, et al. In-flame soot particle structure on the up- and down-swirl side of a wall-interacting jet in a small-bore diesel engine. Proc Combust Inst 2019;37(4):4847–55.
[53] Cheung SCP, Yuen RKK, Yeoh GH. Contribution of soot particles on global radiative heat transfer in a two-compartment fire. Fire Saf J 2004;39(5):412–28.
[54] Jacobson MZ. Strong radiative heating due to the mixing state of black carbon in atmospheric aerosols. Nature 2001;409:695–7.
[55] Liu L, Mishchenko MI, Arnott WP. A study of radiative properties of fractal soot aggregates using the superposition T-matrix method. J Quant Spectrosc Radiat Transf 2008;109:2656–63.
[56] Bond TC, Doherty SJ, Fahey DW, et al. Bounding the role of black carbon in the climate system: a scientific assessment. J Geophys Res Atmos 2013;118(11):5380–552.
[57] Botero ML, Sheng Y, Akroyd J, et al. Internal structure of soot particles in a diffusion flame. Carbon 2019;141:635–42.
[58] Ferraro F, Russo C, Schmitz R, et al. Experimental and numerical study on the effect of oxymethylene ether-3 (OME_3) on soot particle formation. Fuel 2021;286:119353.
[59] Liu Y, Zhang R, Wang J, et al. Soot particles formed by n-heptane and n-heptane/oxymethylene ether-3 in an inverse diffusion flame: a comparative analysis of chemical features. Fuel 2024;366(15):131422.
[60] Alfè M, Apicella B, Barbella R, et al. Structure-property relationship in nanostructures of young and mature soot in premixed flames. Proc Combust Inst 2009;32(1):697–704.
[61] Vander Wal RL, Mueller CJ. Initial investigation of effects of fuel oxygenation on nanostructure of soot from a direct-injection diesel engine. Energy Fuel 2006;20(6):2364–9.
[62] Tree DR, Svensson KI. Soot processes in compression ignition engines. Prog Energy Combust Sci 2007;33(3):272–309.
[63] Michael F. Reaction mechanism of soot formation in flames. PCCP 2002;4(11):2028–37.
[64] Pierson HO. Handbook of carbon, graphite, diamonds and fullerenes. Oxford: William Andrew Publishing; 1994.
[65] Vander Wal RL, Strzelec A, Toops TJ, et al. Forensics of soot: C5-related nanostructure as a diagnostic of in-cylinder chemistry. Fuel 2013:113522–6.
[66] Kroto HW, Heath JR, O'brien SC, et al. C60: Buckminsterfullerene. Nature 1985;318:162–3.
[67] Marsden E. Photoluminescence: advances in research and applications. Nova science publishers; 2018.
[68] Al-Qurashi K, Boehman AL. Impact of exhaust gas recirculation (EGR) on the oxidative reactivity of diesel engine soot. Combust Flame 2008;155(4):675–95.
[69] Ishiguro T, Suzuki N, Fujitani Y, et al. Microstructural changes of diesel soot during oxidation. Combust Flame 1991;85(1–2):1–6.
[70] Zhang W, Song C, Lyu G, et al. Petroleum and Fischer-Tropsch diesel soot: a comparison of morphology, nanostructure and oxidation reactivity. Fuel 2021;283:118919.